

Kalman tracking and estimation of continuous gravitational waves with a pulsar timing array

Kimpson¹, Melatos, O’Leary, Evans, others, etc. etc. ^{★†}

¹*Royal Astronomical Society, Burlington House, Piccadilly, London W1J 0BQ, UK*

Last updated 7 August 2023

ABSTRACT

This is an abstract

Key words: gravitational waves – methods: data analysis – pulsars: general

1 INTRODUCTION

The inspiral of supermassive black hole binaries (SMBHBs; Rajagopal & Romani 1995; Jaffe & Backer 2003; Wyithe & Loeb 2003; Sesana 2013; McWilliams et al. 2014; Ravi et al. 2015; Burke-Spolaor et al. 2019; Sykes et al. 2022) is predicted to emit nHz gravitational waves (GWs). Other GW sources in this low-frequency regime include cosmic strings (e.g. Sanidas et al. 2012) and cosmological phase transitions (e.g. Xue et al. 2021). The detection of nHz GWs has necessitated the development of new observational methods, since it is practically impossible to engineer interferometric detectors with sufficiently long baselines. The foremost method is timing an ensemble of pulsars; a pulsar timing array (PTA; Tiburzi 2018; Verbiest et al. 2021). A nHz GW influences the trajectory and frequency of radio pulses, leaving a characteristic impression on the pulse times of arrival (TOAs) measured at the Earth. By measuring TOAs from multiple pulsars simultaneously one can effectively construct a detector with a baseline on the scale of parsecs. Multiple PTA detectors have been built over the last few decades, including the North American Nanohertz Observatory for Gravitational Waves (NANOGrav, Agazie et al. 2023b), the Parkes Pulsar Timing array (PPTA, Zic et al. 2023), and the European Pulsar Timing Array (EPTA, Antoniadis et al. 2023b). These individual efforts have joined in international collaboration, under the umbrella of the International Pulsar Timing Array (IPTA, Perera et al. 2019), along with a number of newer PTAs such as the Indian Pulsar Timing Array Project (InPTA, Tarafdar et al. 2022), MeerTime (Bailes et al. 2020; Spiwak et al. 2022) and the Chinese PTA (CPTA, Hobbs et al. 2019).

The incoherent superposition of multiple SMBHB sources leads to a stochastic GW background detectable at nHz frequencies (Allen 1997; Sesana et al. 2008; Christensen 2019; Renzini et al. 2022). Previous efforts have mainly focused on detecting the stochastic background by measuring the cross-correlation between the pulsar timing residuals between pairs of pulsars as a function of the angular separation between the pulsars – the Hellings-Downs curve

(Hellings & Downs 1983). After multiple non-detections (Lentati et al. 2015; Arzoumanian et al. 2018b; Antoniadis et al. 2022) consistent evidence for the GW background was presented by NANOGrav (Agazie et al. 2023a), EPTA/InPTA (Antoniadis et al. 2023a), PPTA (Reardon et al. 2023) and the CPTA (Xu et al. 2023)

Individual SMBHBs that are sufficiently massive and nearby may be resolvable with PTAs, allowing the very earliest stages of their evolution and coalescence to be investigated (Sesana & Vecchio 2010; Yardley et al. 2010; Zhu et al. 2015a; Babak & Sesana 2012; Ellis 2013; Zhu et al. 2016). Indeed, the stochastic GW background itself may be dominated by a few individual binary sources (Ravi et al. 2012). Individual SMBHBs are continuous wave sources: they generate persistent, quasi-monochromatic modulations of a known form in pulsar timing residuals. Consequently, they are detected more efficiently by either a frequentist matched filter e.g. the \mathcal{F} -statistic (Lee et al. 2011; Ellis et al. 2012; Zhu et al. 2014) or else Bayesian inference (Ellis & Cornish 2016; Arzoumanian et al. 2020a) rather than by cross-correlating pulsar pairs. However, PTA observational efforts to detect individual sources have thus far been unsuccessful (Jenet et al. 2004; Zhu et al. 2014; Babak et al. 2016; Arzoumanian et al. 2023), with inconclusive evidence at low significance presented by the EPTA for a individual source at 4–5 nHz (Antoniadis et al. 2023c).

Intrinsic pulsar timing noise – i.e. random, unmodelled, red-spectrum TOA fluctuations due to irregularities in the rotation of the star – has been identified as a key factor limiting the sensitivity of PTAs to GW signals (Shannon & Cordes 2010a; Lasky et al. 2015; Caballero et al. 2016; Goncharov et al. 2021). This timing noise has multiple theorized causes including free precession (Kerr et al. 2015; Stairs et al. 2000), microglitches (D’Alessandro et al. 1995; Melatos et al. 2008; Espinoza et al. 2021), asteroid encounters (Shannon et al. 2013; Brook et al. 2013), glitch recovery (Johnston & Galloway 1999; Hobbs et al. 2010), fluctuations in internal and external stochastic torques (Cordes & Greenstein 1981; Urama et al. 2006; Antonelli et al. 2023), variations in the coupling between the stellar crust and core (Jones 1990; Meyers et al. 2021b; Melatos et al. 2021), magnetospheric state switching (Kramer et al. 2006; Lyne et al. 2010; Stairs et al. 2019) and superfluid turbulence (Greenstein 1970; Peralta et al. 2006; Melatos & Link 2014). In

[★] Contact e-mail: tom.kimpson@unimelb.edu.au

[†] Present address: Science magazine, AAAS Science International, 82-88 Hills Road, Cambridge CB2 1LQ, UK

order to mitigate the impact of timing noise, PTAs are typically composed of millisecond pulsars (MSPs) which are relatively stable rotators. However, timing noise in MSPs may be a latent phenomenon that will increasingly assert itself as longer stretches of more sensitive data are analysed in the quest to detect nHz GWs (Shannon & Cordes 2010a). In modern Bayesian PTA searches, the power spectral density of the intrinsic timing noise is modeled (usually as a broken or unbroken power law) and estimated, in an effort to distinguish it from the red noise induced by a stochastic GW background (whose spectrum is also red). In addition to the red timing noise there are also secondary, white noise sources that must be considered such as phase jitter noise and radiometer noise (Cordes & Shannon 2010; Lam et al. 2019; Parthasarathy et al. 2021).

In this work we present an alternative and complementary approach to PTA data analysis for individual, quasi-monochromatic, SMBHB sources which self-consistently tracks the intrinsic timing noise in PTA pulsars and disentangles it from GW-induced TOA modulations. The new approach differs from existing approaches in one key respect: it infers the GW parameters conditional on the unique, time-ordered realization of the noisy TOAs observed, instead of fitting for the ensemble-averaged statistics of the TOA noise process, e.g., the amplitude and exponent of its power spectral density. Stated another way, existing approaches seek to detect a GW signal by marginalizing over the ensemble of possible noise realizations, whereas the new approach delivers the most likely set of GW parameters consistent with the actual, observed noise realization. The new and existing approach are therefore complementary, but the new approach holds out the promise of somewhat higher sensitivity — a promise which we aim to test as the key goal of this paper. In particular, we formulate PTA analysis as a state-space problem and demonstrate how to optimally estimate the state-space evolution using a Kalman filter, a tried-and-tested tool (Kalman 1960; Meyers et al. 2021b; Melatos et al. 2021). We combine the Kalman tracking of the pulsars intrinsic rotational state with a Bayesian nested sampler (Skilling 2006; Ashton et al. 2022) to estimate the GW parameters and calculate the marginal likelihood for model selection.

This paper is organised as follows. In Section 2 we present the state-space model for the pulsar pulse frequency which is subject to the influence of a GW. In Section 3 we discretise the model, develop a Kalman filter to track the state evolution and introduce how to deploy the Kalman filter in conjunction with nested sampling to estimate the system parameters and the model evidence. **TK: this paper outline section will be completed once we have finalized the rest of the manuscript** In Section 4 we test this new method on synthetic pulsar data. Throughout this work we adopt the natural units, with $c = G = \hbar = 1$, and a $(-, +, +, +)$ metric signature.

2 STATE-SPACE FORMULATION

We formulate the PTA analysis as a state-space problem, in which the intrinsic rotational state of each pulsar evolves according to a stochastic differential equation and is related to the observed pulse sequence via a measurement equation. In this work we take the intrinsic state variable to be the pulsar’s spin frequency $f_p^{(n)}(t)$, as measured in the local rest frame of the pulsar’s centre of mass. A model for the evolution of $f_p^{(n)}(t)$ is presented in Section 2.1. We take the measurement variable to be the radio pulse frequency measured by an observer at Earth, $f_m^{(n)}(t)$. The measurement equation relating

$f_m^{(n)}(t)$ to $f_p^{(n)}(t)$ is presented in Section 2.2. The superscript $1 \leq n \leq N$ indexes the n -th pulsar in the array.

2.1 Spin evolution

A predictive, first-principles theory of timing noise does not exist at present; there are several plausible physical mechanisms, referenced in Section 1. We therefore rely on an idealized phenomenological model to capture the main qualitative features of a typical PTA pulsar’s observed spin evolution, i.e. random, small-amplitude excursions around a smooth, secular trend. In the model, $f_p^{(n)}(t)$ evolves according to the sum of a deterministic torque and a stochastic torque. The deterministic torque is attributed to magnetic dipole braking, with braking index $n_{\text{em}} = 3$. Most PTAs involve millisecond pulsars, for which the quadratic correction due to n_{em} in $f_p^{(n)}(t)$ is negligible over the observation time $T_{\text{obs}} \sim 10$ yr, and the deterministic evolution can be approximated accurately by

$$f_{\text{em}}^{(n)}(t) = f_{\text{em}}^{(n)}(t_1) + \dot{f}_{\text{em}}^{(n)}(t_1)t, \quad (1)$$

where an overdot denotes a derivative with respect to t and t_1 labels the time of the first TOA. The stochastic torque is assumed to be a zero-mean white noise process. Specifically, the frequency evolves according to an Ornstein-Uhlenbeck process, described by a Langevin equation with a time-dependent drift term (Vargas & Melatos 2023)

$$\frac{df_p^{(n)}}{dt} = -\gamma^{(n)}[f_p^{(n)} - f_{\text{em}}^{(n)}(t)] + \dot{f}_{\text{em}}^{(n)} + \xi^{(n)}(t). \quad (2)$$

In Eq 2, f_{EM} is the solution of the electromagnetic spindown equation, \dot{f}_{EM} is the spin derivative, $\gamma^{(n)}$ a proportionality constant whose reciprocal specifies the mean-reversion timescale, and $\xi^{(n)}(t)$ satisfies:

$$\langle \xi^{(n)}(t) \rangle = 0, \quad (3)$$

$$\langle \xi^{(n)}(t) \xi^{(n)}(t') \rangle = [\sigma^{(n)}]^2 \delta(t - t'). \quad (4)$$

$[\sigma^{(n)}]^2$ is the variance of $\xi^{(n)}$ and parametrizes the amplitude of the noise, and combined with the mean reversion it gives a characteristic root mean square fluctuations $\approx [\sigma^{(n)}]^2 / \gamma^{(n)}$ in $f_p^{(n)}(t)$ (Gardiner 2009). It is important to note that the white noise fluctuations in $\xi(t)$ translate into red noise fluctuations in the rotational phase $\phi(t) = \int_{t_1}^t dt' f_p(t')$ after being filtered by the terms involving d/dt and γ in Eq. 1, consistent with the observed power spectral density of typical millisecond pulsars in the nHz band relevant to PTA experiments.

Equations 1–4 represent a phenomenological model, which aims to reproduce qualitatively the typical timing behaviour observed in PTAs, viz. a mean-reverting random walk about a secular spin-down trend [ref latest results paper from each of the three main PTAs]. Equations 1–4 are not derived from first principles by applying a microphysical theory. As a first pass, they also exclude certain phenomenological elements, which are likely to be present in reality, e.g. the classic, two-component, crust-superfluid structure inferred from post-glitch recoveries (Baym et al. 1969; van Eysden & Melatos 2010; Gügercinoğlu & Alpar 2017). An approach akin to Equations 1–4 has been followed successfully in other timing analyses in the context of anomalous braking indices (Vargas & Melatos 2023) and hidden Markov model glitch searches (Melatos et al. 2020; Lower

et al. 2021; Dunn et al. 2022, 2023). However, Equations 1–4 involve significant idealizations, which must be recognized at the outset (Meyers et al. 2021b,a; Vargas & Melatos 2023). First, the white noise driver $\xi(t)$ in Equation 2 is not differentiable, which makes the formal interpretation of $d^2 f_p/dt^2$ ambiguous, even though $d^2 f_p/dt^2$ is not used in the PTA analysis proposed in this paper. Second, the white spectrum assumed for $\xi(t)$ may or may not be suitable for millisecond pulsars in PTAs. It is challenging observationally to infer the spectrum of $\xi(t)$ from the observed spectrum of the phase residuals, because the inference is conditional on the (unknown) dynamical model governing df_p/dt . For small-amplitude fluctuations sampled relatively often, as in millisecond pulsars in PTAs, it is likely that $\xi(t)$ is white to a good approximation over the inter-TOA intervals and generates red phase residuals as observed, but caution is warranted nevertheless. Third, the Brownian increment $dB(t) = \xi(t)dt$ does not include non-Gaussian excursions such as Lévy flights (Sornette 2004) which have not been ruled out by pulsar timing experiments to date. The above three idealizations are supplemented by other, physical approximations noted above, e.g. neglecting n_{em} in Equation 1 and differential rotation between the crust and superfluid in Equation 2.

2.2 Modulation of pulse TOAs by a GW

In the presence of a GW, the pulse frequency measured by an observer in the local rest frame of the neutron star’s center of mass is different from that measured by an observer on Earth. Indeed, the pulse TOAs are modulated harmonically at the GW frequency. We derive the nonlinear measurement equation relating $f_m(t)$ to $f_p(t)$ in this section. The measurement equation is a key input into the Kalman filter in Section 3.1

2.2.1 Plane GW perturbation

We consider a gravitational plane wave from a single, distant source, which perturbs a background Minkowski metric $\eta_{\mu\nu}$ as

$$g_{\mu\nu} = \eta_{\mu\nu} + H_{\mu\nu} \exp[i(\Omega(\mathbf{n} \cdot \mathbf{x} - t) + \Phi_0)], \quad (5)$$

with spatial coordinates \mathbf{x} and global coordinate time t . The GW has a constant angular frequency Ω , propagates in the \mathbf{n} -direction (where \mathbf{n} is a unit vector), has amplitude tensor $H_{\mu\nu}$, and has a phase offset Φ_0 . Throughout this paper we work with pulsar TOAs which have been defined relative to the Solar System barycentre (SSB). We are free to choose our coordinate system such that Φ_0 is the GW phase at $t = 0$ at the SSB. In this paper Ω has no time dependence; the source is approximated as monochromatic. Studies of SMBHB inspirals in the PTA context show that the gravitational wave frequency f_{gw} ($= \Omega/2\pi$) evolves over decadal timescales as (e.g. Zhu et al. 2015a),

$$\Delta f_{\text{gw}} \simeq 3.94 \text{ nHz} \left(\frac{M_c}{10^9 M_\odot} \right)^{5/3} \left(\frac{f_{\text{gw}}(t=0)}{10^{-7} \text{ Hz}} \right)^{11/3} \left(\frac{T_{\text{obs}}}{10 \text{ yr}} \right) \quad (6)$$

where M_c is the chirp mass of the SMBHB, $f_{\text{gw}}(t=0)$ is the GW frequency at the time of the first observation, and T_{obs} the length of the data timespan, which for PTAs is ~ 10 years. A source can be considered as monochromatic if Δf_{gw} is less than the PTA frequency resolution of $1/T_{\text{obs}}$. From Eq. 6 we can see that only those binaries which are very massive or at very high frequency experience significant frequency evolution over typical PTA timespans. The majority of SMBHBs detectable with PTAs are expected to satisfy $\Delta f_{\text{gw}} < 1/T_{\text{obs}}$; for a PTA with pulsars at 1.5 kpc, 78 % of simulated SMBHBs satisfy this condition for the current IPTA, whilst for the

second phase of the Square Kilometer Array (SKA2) this fraction drops to 52 % (Fig 7 of Rosado et al. 2015). We are therefore justified in treating the GW source as monochromatic (Sesana et al. 2008; Sesana & Vecchio 2010; Ellis et al. 2012).

The amplitude tensor $H_{\mu\nu}$ has zero temporal components ($H_{0\mu} = H_{\mu 0} = 0$). The spatial part is

$$H_{ij} = h_+ e_{ij}^+(\mathbf{n}) + h_\times e_{ij}^\times(\mathbf{n}), \quad (7)$$

where h_+ and h_\times are the respective polarisation amplitudes. The plus and cross polarisation tensors e_{ij}^+ and e_{ij}^\times are uniquely defined by the principal axes of the wave, viz. the unit 3-vectors \mathbf{k} and \mathbf{l} , according to

$$e_{ij}^+(\mathbf{n}) = k_i k_j - l_i l_j, \quad (8)$$

$$e_{ij}^\times(\mathbf{n}) = k_i l_j + l_i k_j. \quad (9)$$

The principal axes are in turn specified by the location of the GW source on the sky (via colatitude θ and azimuth ϕ) and the polarisation angle ψ according to

$$\begin{aligned} \mathbf{k} = & (\sin \phi \cos \psi - \sin \psi \cos \phi \cos \theta) \hat{\mathbf{x}} \\ & - (\cos \phi \cos \psi + \sin \psi \sin \phi \cos \theta) \hat{\mathbf{y}} \\ & + (\sin \psi \sin \theta) \hat{\mathbf{z}} \end{aligned} \quad (10)$$

$$\begin{aligned} \mathbf{l} = & (-\sin \phi \sin \psi - \cos \psi \cos \phi \cos \theta) \hat{\mathbf{x}} \\ & + (\cos \phi \sin \psi - \cos \psi \sin \phi \cos \theta) \hat{\mathbf{y}} \\ & + (\cos \psi \sin \theta) \hat{\mathbf{z}} \end{aligned} \quad (11)$$

where e.g. $\hat{\mathbf{x}}$ is a unit vector in the direction of the x -axis. The direction of GW propagation is related to the principal axes by

$$\mathbf{n} = \mathbf{k} \times \mathbf{l}. \quad (12)$$

2.2.2 Measurement equation

TK: Does this subsection needs a better name?

TK: this subsection has been overhauled per comments from AM. The structure is now:

1. Radio pulses described by general geometric object p
2. Shift in p due to a GW (no derivation, just definition of terms)
3. Relate shift in p to a shift in f by clarifying that $u = (1, 0, 0, 0)$ for PSR and observer.
4. Give final measurement equation

In general radio pulses from a pulsar are transmitted as amplitude modulations of a radio-frequency carrier wave. They are described by the geometric object \vec{p} which we can identify as the 4-momentum of the radio photon. The presence of a GW induces a shift in the temporal component of the covariant 4-momentum between the emitter and the observer, i.e. $\Delta p_t = p_t|_{\text{observer}} - p_t|_{\text{emitter}}$, as (e.g. Maggiore 2018)

$$\Delta p_t = \frac{\omega}{2} \frac{h_{ij}(t; \mathbf{x}=0) q^i q^j}{(1 + \mathbf{n} \cdot \mathbf{q})} \left(1 - e^{i\Omega(1 + \mathbf{n} \cdot \mathbf{q})d} \right) \quad (13)$$

where ω is the angular pulse frequency ($= 2\pi f_p$) measured in the momentarily comoving reference frame (MCRF) of an observer, $h_{ij} = g_{ij} - \eta_{ij}$, \mathbf{q} is the unit vector connecting the observer and the pulsar and d is the distance to the pulsar. We take the pulsar location to be constant i.e. \mathbf{q} is not a function of time. In practice the pulsar locations vary with respect to the Earth but are constant with respect to the SSB. This barycentering correction is typically applied when generating TOAs using e.g. TEMPO2 and related timing

software. Generally the measured frequency of a photon recorded by an observer who is travelling with 4-velocity \vec{u} is given by the coordinate-independent expression:

$$f = p_\alpha u^\alpha . \quad (14)$$

Due to the kinematical corrections from the barycentering process,

$$u^\alpha|_{\text{emitter}} = u^\alpha|_{\text{receiver}} = (1, 0, 0, 0) \quad (15)$$

where the perturbations to \vec{u} from the GW are of higher order and neglected. In this case the shift in the momentum from Equation 13 can be related to a shift in the frequency as,

$$f_m^{(n)}(t) = f_p^{(n)}(t - d)g^{(n)}(t) \quad (16)$$

where **TK: what is the best notation here to give q^i an (n) superscript?**

$$g^{(n)}(t) = 1 - \frac{1}{2} \frac{h_{ij}(t; \mathbf{x} = 0) q_{(n)}^i q_{(n)}^j}{(1 + \mathbf{n} \cdot \mathbf{q}^{(n)})} \left(1 - e^{i\Omega(1 + \mathbf{n} \cdot \mathbf{q}^{(n)})d^{(n)}} \right) . \quad (17)$$

It is will also prove instructive to express Eq. 17 in a trigonometric form as, or in a trigonometric form

$$g^{(n)}(t) = 1 - \frac{1}{2} \frac{H_{ij} q_{(n)}^i q_{(n)}^j}{(1 + \mathbf{n} \cdot \mathbf{q}^{(n)})} \times \left[\cos(-\Omega t + \Phi_0) - \cos\left(-\Omega t + \Phi_0 + \Omega \left(1 + \mathbf{n} \cdot \mathbf{q}^{(n)}\right) d^{(n)}\right) \right] . \quad (18)$$

Equations 16, 18, 17 define a measurement equation that relates the intrinsic pulsar spin frequency to the radio pulse frequency measured by an observer on Earth.

3 SIGNAL TRACKING AND PARAMETER ESTIMATION

The set of static parameters θ of the model outlined in Section 2 can be separated into parameters which correspond to the intrinsic frequency evolution of the pulsar and parameters of the GW source, i.e.

$$\theta = \theta_{\text{psr}} \cup \theta_{\text{gw}} , \quad (19)$$

with

$$\theta_{\text{psr}} = \left\{ \gamma^{(n)}, f_{\text{em}}^{(n)}(t_1), \dot{f}_{\text{em}}^{(n)}(t_1), d^{(n)}, \sigma^{(n)} \right\}_{1 \leq n \leq N} , \quad (20)$$

and

$$\theta_{\text{gw}} = \{h_0, \iota, \delta, \alpha, \psi, \Omega, \Phi_0\} . \quad (21)$$

In Eq 21 we have reparameterized the two GW polarisation strains, h_+ , h_\times , in terms of the GW amplitude h_0 and the system inclination ι :

$$h_+ = h_0(1 + \cos^2 \iota) , \quad (22)$$

$$h_\times = -2h \cos \iota , \quad (23)$$

where ι is the angle between the normal to the SMBHB orbital plane, \mathbf{L} , and the observer line of sight, i.e. $\cos \iota = \mathbf{n} \cdot \mathbf{L}$. We use this parametrisation in terms of h_0 and ι throughout the remainder of this work. For a PTA dataset containing N pulsars we then have $7 + 5N$ parameters to estimate. Typically the pulsar parameters are better constrained than the GW parameters; for example estimates of pulsar distances are accurate to $\sim 10\%$ (Cordes & Lazio 2002; Verbiest et al. 2012; Desvignes et al. 2016; Yao et al. 2017),

but we have no prior information on the SMBHB GW source location.

In this section we present a new method to infer θ and calculate the marginal likelihood (i.e. the model evidence). In Section 3.1 we outline how noisy measurements of the pulsar frequency, $f_m^{(n)}(t)$, can be used to estimate the hidden state sequence, $f_p^{(n)}(t)$, using a Kalman filter. In Section 3.2 we demonstrate how to deploy the Kalman filter in conjunction with a nested sampling technique to perform Bayesian inference of the model parameters and calculate the model evidence. Model selection and the specification of the null model is described in Section 3.3.

3.1 Kalman filter

The Kalman filter (Kalman 1960) is an algorithm for recovering the most likely evolution of a set of system state variables, \mathbf{X} , given some noisy measurements, \mathbf{Y} . It is a common technique in signal processing that has been applied successfully in neutron star astrophysics (e.g. Meyers et al. 2021b; Melatos et al. 2021). In this work we use the linear Kalman filter which assumes a linear relation between \mathbf{X} and \mathbf{Y} . Whilst the measurement equation, Eq. 16, is non-linear in the static parameters it is linear in the state and measurement variables, $f_p^{(n)}$ and $f_m^{(n)}$ respectively. Extension to non-linear problems is straightforward using either an extended Kalman filter (Zarchan & Musoff 2000), the unscented Kalman filter (Wan & Van Der Merwe 2000) or the particle filter (Simon 2006).

The full set of Kalman recursions is presented in Appendix A. At each discrete timestep $i = 1, \dots, M$, the Kalman filter returns an estimate of the state variables, $\hat{\mathbf{X}}_i$, and the covariance of those estimates, \mathbf{P}_i . The filter tracks the error in its predictions of \mathbf{X}_i by projecting the state predictions back into measurement space, $\hat{\mathbf{X}}_i \mapsto \hat{\mathbf{Y}}_i$, via the measurement equation, Eq. 16. The measurement predictions can then be compared against the true observed noisy measurements to get a residual $\epsilon_i = \mathbf{Y}_i - \hat{\mathbf{Y}}_i$, sometimes termed the ‘‘innovation’’. The Kalman filter also calculates the uncertainty in ϵ_i via the innovation covariance $\mathbf{S}_i = \langle \epsilon_i \epsilon_i^\top \rangle$. The Gaussian log-likelihood can then be calculated at each timestep:

$$\log \mathcal{L}_i = -\frac{1}{2} \left(N \log 2\pi + \log |\mathbf{S}_i| + \epsilon_i^\top \mathbf{S}_i^{-1} \epsilon_i \right) , \quad (24)$$

with the total log-likelihood simply the sum over all timesteps, i.e.

$$\log \mathcal{L} = \sum_{i=1}^M \log \mathcal{L}_i . \quad (25)$$

For fixed data \mathbf{Y} , \mathcal{L} is a function of the static parameters of the model, i.e. $\mathcal{L} = \mathcal{L}(\mathbf{Y}|\theta)$. Similarly the estimates of the state and measurement variables, $\hat{\mathbf{X}}$ and $\hat{\mathbf{Y}}$, are also functions of θ . If the estimates of the system parameters, $\hat{\theta}$, that we pass to the Kalman filter are close to the true underlying parameters then the error in $\hat{\mathbf{X}}$, $\hat{\mathbf{Y}}$ is minimized and \mathcal{L} is maximised. This is illustrated in Figure 1a; given a data timeseries of the measured pulsar frequency the Kalman filter is able to recover the evolution of the hidden state with high fidelity. The residuals correspond to random noise and are normally distributed. Conversely, if $\hat{\theta}$ is not close to the true parameters then the filter is unable to recover the state evolution. This is demonstrated in Figure 1b where the Kalman filter was run with $\hat{\theta}$ slightly perturbed away from the true values. In this case the filter cannot track the state variable accurately and the residuals are no longer Gaussian.

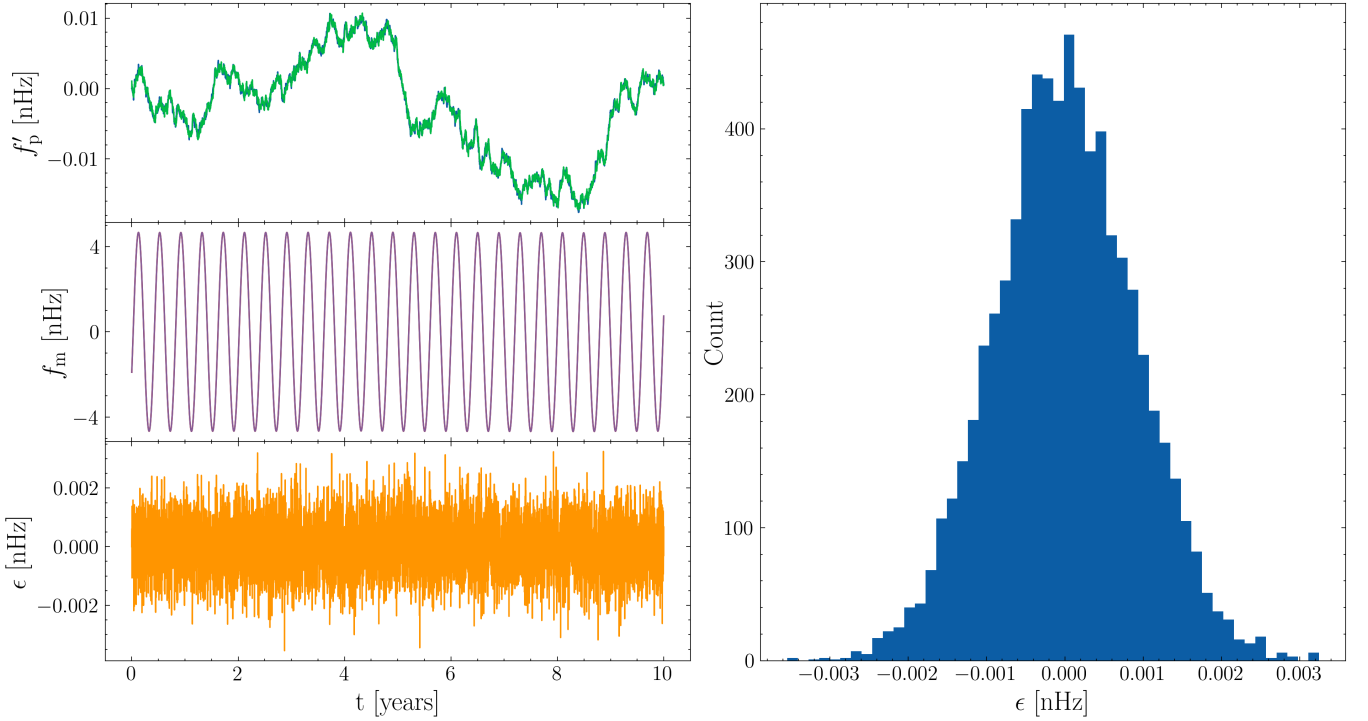
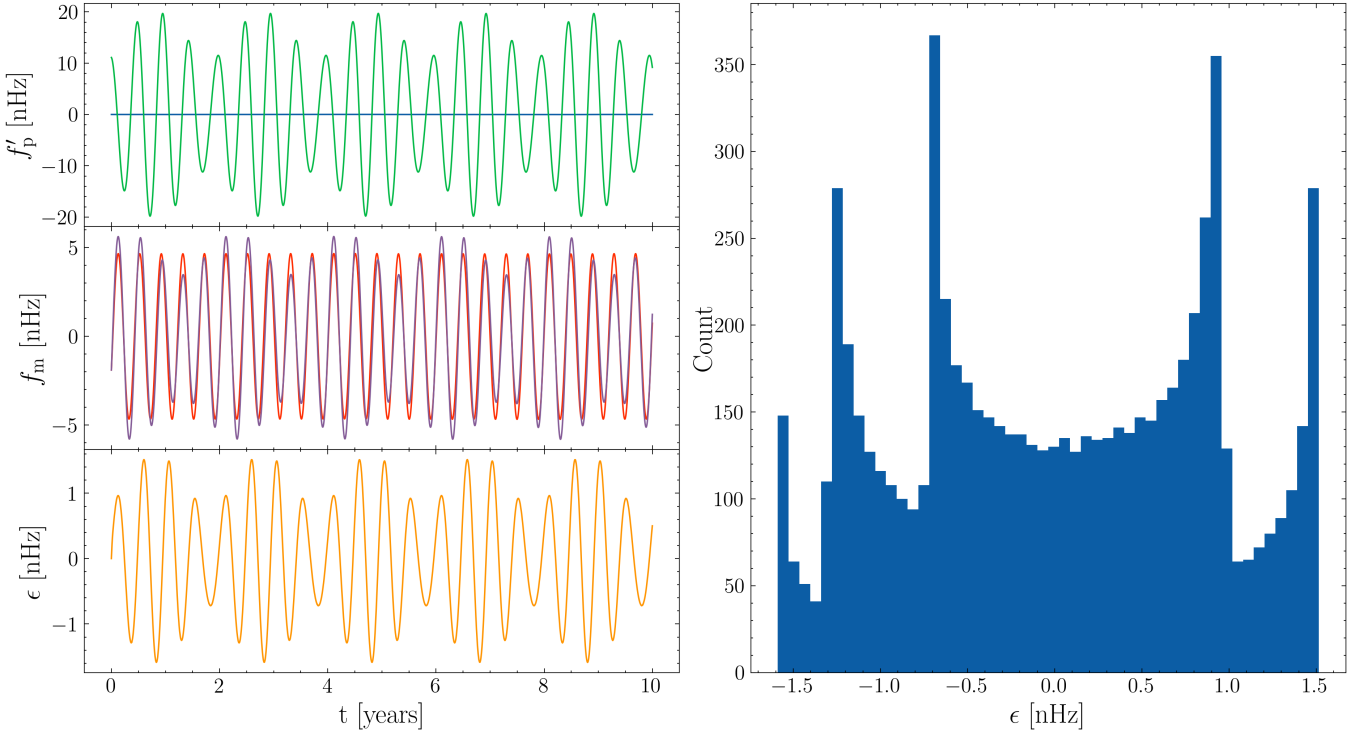

 (a) Kalman filter using correct estimate of the static parameters, $\hat{\theta} = \theta$

 (b) Kalman filter using incorrect estimate of the static parameters, $\hat{\theta} \neq \theta$

Figure 1. Example application of a Kalman filter to estimate the intrinsic pulsar frequency state $f_p(t)$ given a measured frequency $f_m(t)$. We here plot the ephemeris subtracted state $f'_p(t) = f_p(t) - f_{em}(t)$ to better illustrate the stochastic wandering of the pulsar frequency. In (a) the Kalman filter is run using identically correct estimates of the static system parameters, $\hat{\theta} = \theta$ and the state is estimated accurately. In (b) the Kalman filter is run with $\hat{\theta} \neq \theta$ and the state is not estimated accurately. The top left panels show the true pulsar state $f'_p(t)$ (blue line) and the state estimated by the Kalman filter, $\hat{f}'_p(t)$ (green line). The middle left panels show the true $f_m(t)$ (red line) and the measured frequency estimated by the Kalman filter, $\hat{f}_m(t)$ (magenta). The bottom left panels show the residual or the innovation $\epsilon(t) = f_m(t) - \hat{f}_m(t)$. The right hand panels plot the distribution of the innovation over the total observation period.

3.2 Nested Sampling

We can use the likelihood returned by the Kalman filter, Eq 25, in conjunction with likelihood-based inference methods to estimate the posterior distribution of θ by Bayes' Rule,

$$p(\theta|Y) = \frac{\mathcal{L}(Y|\theta) \cdot \pi(\theta)}{\mathcal{Z}} \quad (26)$$

where $\pi(\theta)$ is the prior distribution on θ and \mathcal{Z} is the marginalised likelihood, or evidence

$$\mathcal{Z} = \int \mathcal{L}(Y|\theta) \pi(\theta) d\theta. \quad (27)$$

In order to estimate the posterior distribution and the model evidence we use nested sampling (Skilling 2006) throughout this work. Nested sampling is an integration algorithm used for evaluating marginalised likelihood integrals, of the form given by Eq. 27, that also returns samples from the posterior, $p(\theta|Y)$. It does this by drawing a set of n_{live} live points from $\pi(\theta)$ and then iteratively replacing the live point with the lowest likelihood with a new live point drawn from $\pi(\theta)$, where the new live point is required to have a higher likelihood than the discarded point. The primary advantage of nested sampling is the ability to compute the evidence integral, which is key for model selection, and proves difficult without considerable extra cost for the usual Markov Chain Monte Carlo (MCMC) approaches. Nested sampling is also typically less computationally intensive than MCMC and can handle multi-modal problems (Ashton et al. 2022). For these reasons, it has enjoyed widespread adoption in the physical sciences, particularly within the cosmological community (Mukherjee et al. 2006; Feroz & Hobson 2008; Handley et al. 2015), but has also commonly been applied in astrophysics (Buchner 2021b), particle physics (Trassinelli 2019) and materials science (Pártay et al. 2009). For a review of nested sampling we refer the reader to Buchner (2021a) and Ashton et al. (2022). Multiple nested sampling algorithms and computational libraries exist. (e.g. Feroz & Hobson 2008; Feroz et al. 2009; Handley et al. 2015; Speagle 2020; Buchner 2021b). For gravitational astrophysics it is common to use the dynesty sampler (Speagle 2020) via the Bilby Ashton & Talbot (2021) front-end library. We follow this precedent and use Bilby for all nested sampling Bayesian inference in this work. The primary tunable parameter in nested sampling is n_{live} , where a greater number of live points is advantageous for large parameter spaces and multi-modal problems, whilst the uncertainties in the evidence and the posterior scale as $\mathcal{O}(1/\sqrt{n_{\text{live}}})$. However the computational run-time scales as $\mathcal{O}(n_{\text{live}})$ and so one must make a trade-off between uncertainty and runtime. Ashton et al. (2022) offer a rule-of-thumb where the minimum number of live points should be greater than the number of static parameters. The results presented in this work are generally robust to the choice of n_{live} , subject to the requirement of $n_{\text{live}} > 7 + 5N$. We take $n_{\text{live}} = 500$ for all results presented in this work.

3.3 Model selection

The evidence integral, \mathcal{Z} , returned by nested sampling is the probability of the data Y given a particular model \mathcal{M}_i . This enables us to compare competing models via a Bayes factor,

$$\beta = \frac{\mathcal{Z}(Y|\mathcal{M}_1)}{\mathcal{Z}(Y|\mathcal{M}_0)}. \quad (28)$$

Throughout this work we take \mathcal{M}_1 to be the complete model defined in Section 2. \mathcal{M}_0 is our null model that assumes there is no GW in the data. This is equivalent to setting $g^{(n)}(t) = 1$ in Equation 17, 18.

The Bayes factors we quote in this work therefore quantify whether the data supports evidence for a GW compared to there being no GW signal present.

4 TESTS WITH SYNTHETIC DATA

In this section we use synthetic data to test the ability of our method to detect the presence of a GW in noisy data and recover the static parameters, θ . In Section 4.1 we discuss how the synthetic data is generated, including the construction of an artificial PTA. In Section 4.2 we generate synthetic data for a single representative example SMBHB system and apply our method to estimate θ and calculate the statistical evidence for a GW in the data via the Bayes factor. In this section we also explore how the detectability of the system changes for different magnitudes of h_0 . In Section 4.3 we move beyond a single example system and explore a broader parameter space...

4.1 Synthetic data generation

4.1.1 Constructing a synthetic PTA

For this work we generate representative synthetic data as follows. We first specify a set of pulsars to make up our artificial PTA. We take the 47 pulsars that make up the 12.5 year NANOGrav PTA (Arzoumanian et al. 2020b). For each pulsar we obtain the sky location (which defines the vector \mathbf{q}^n), the distance, the barycentric rotation frequency - which we identify with $f_{\text{em}}^{(n)}(t_1)$ - and the time derivative of the barycentric rotation frequency - which we identify with $\dot{f}_{\text{em}}^{(n)}(t_1)$. The spatial distribution and the distances of the pulsars used for this artificial PTA are shown in Fig 2. The data is acquired via the Australia Telescope National Facility pulsar catalogue (Manchester et al. 2005) using the psrqpy package (Pitkin 2018). The remaining unspecified pulsar parameters are $\gamma^{(n)}$ and $\sigma^{(n)}$. We discussed in Section 2.1 how the quantity $[\sigma^{(n)}]^2/\gamma^{(n)}$ sets the amplitude of the characteristic root mean square fluctuations in $f_p^{(n)}(t)$. Typically the mean reversion timescale $[\gamma^{(n)}]^{-1} \gg T_{\text{obs}}$ (Vargas & Melatos 2023), whilst $[\sigma^{(n)}]^2$ varies between individual pulsars. For this work we fix $\gamma^{(n)} = 10^{-13} \text{ s}^{-1}$ for all n . In order to set a

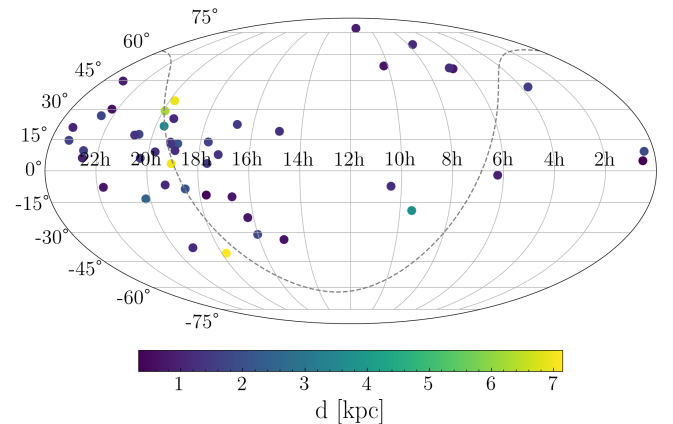


Figure 2. Spatial distribution of 47 pulsars from the 12.5 year NANOGrav data release that make up the synthetic PTA used in this work. The pulsar distances relative to the observer are also indicated, with the majority of pulsars having a distance ~ 1 kpc. The grey dashed line denotes the Galactic plane.

physically reasonable value for $[\sigma^{(n)}]^2$ we use two complementary approaches. The first approach uses the empirical timing noise model from [Shannon & Cordes \(2010b\)](#) where the standard deviation in the pulsar TOA is given by:

$$\ln\left(\frac{\sigma_{\text{TOA}}^{(n)}}{\mu\text{s}}\right) = \ln\alpha_1 + \alpha_2 \ln f_p^{(n)} + \alpha_3 \ln\left(\frac{f_p^{(n)}}{10^{-15}\text{s}^{-2}}\right) + \alpha_4 \ln\left(\frac{T}{1\text{ year}}\right), \quad (29)$$

where T is the length of the observation span and for MSPs $\ln\alpha_1 \sim -20$, $\alpha_2 \sim 1$, $\alpha_3 \sim 2$ and $\alpha_4 \sim 2.4$. Throughout this work we assume that all pulsars are observed with a weekly cadence i.e. $T = 1$ week. The frequency noise parameter can then be calculated for each pulsar where the standard deviation in the pulsar TOA can be related to the standard deviation in the pulsar frequency as

$$\sigma^{(n)} \sim \sigma_{\text{TOA}}^{(n)} \frac{f_p^{(n)}}{T}. \quad (30)$$

For our synthetic NANOGrav PTA, the median $\sigma^{(n)}$ calculated in this way is 4.28×10^{-21} s.

As a sanity check, we can also calculate $\sigma^{(n)}$ using a complementary numerical approach to the empirical best-fit model outlined above. We can directly solve the state equation Eq. 1 numerically using the *baboo* package¹ so as to obtain a synthetic phase solution,

$$\phi^{(n)}(t) = \int_0^t dt' f_p^{(n)}(t'), \quad (31)$$

and generate TOAs and phase residuals. We calibrate the noise amplitude $\sigma^{(n)}$ to generate phase residuals that qualitatively resemble empirical phase residuals measured from real pulsars. We obtain empirical phase residuals from the NANOGrav 12.5 year narrowband data set [Alam et al. \(2021\)](#). For the purposes of validating the $\sigma^{(n)}$ inferred from Eq 30, it is sufficient at this stage to simply compare the synthetic and real phase residuals visually. Whilst it would also be possible to e.g. define some quantitative loss function (e.g. mean-squared error) between the two solutions and solve the optimisation problem to infer $\sigma^{(n)}$, for our purposes this is excessive. It is satisfactory to simply qualitatively compare the two solutions as a useful sanity check. We emphasise that we are not overly concerned with calculating the maximally accurate values for $\sigma^{(n)}$, but instead some reasonable values for constructing representative synthetic data. This approach of generating synthetic phase solutions and visually comparing with empirical solutions is also followed in [Vargas & Melatos \(2023\)](#). In Figure 3 we compare the synthetic and empirical residuals for 3 NANOGrav pulsars: J0030+0451, J0340+4130 and J0613-0200. We can see that for all pulsars the synthetic and empirical residuals are qualitatively similar with the magnitude of the residuals being directly comparable for each pulsar.

4.1.2 Synthetic data generation

We generate N synthetic noisy timeseries - one for each pulsar - as follows:

(i) Integrate the state equations, Eq 1-4 numerically for the synthetic PTA described in Section 4.1.1.

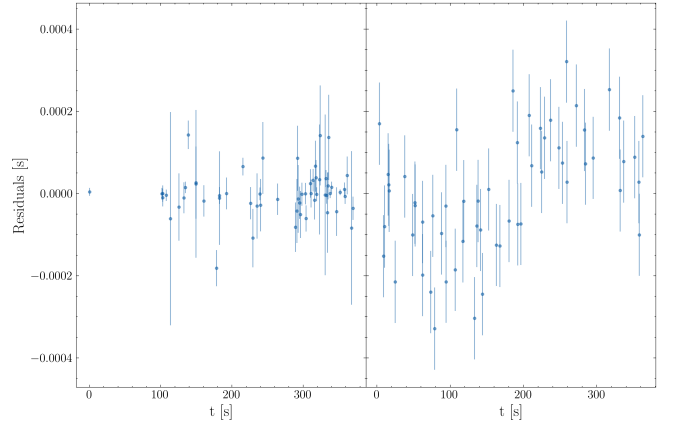


Figure 3. Actual (left panels) and synthetic (right panels) phase residuals for 3 NANOGrav pulsars. The actual residuals are obtained via the NANOGrav 12.5 year data release ([Alam et al. 2021](#)). The synthetic residuals are generated by numerically solving Eq. 1 with $\gamma^{(n)} = 10^{-13}$ and $\sigma^{(n)}$ inferred from Eqs. 29, 30. For all pulsars the two solutions are qualitatively similar, with comparable magnitudes in the residuals. **TK: these plots need updating, but need to discuss with Andres re use of baboo. Maybe just one is sufficient just as an example.**

(ii) Map from state space to measurement space via the measurement equation, Eq. 16

(iii) Add zero-mean Gaussian measurement noise to each time-series, i.e. $f_m^{(n)} + N_f^{(n)}$ where $\langle N_f(t)N_f(t') \rangle = \sigma_m^2 \delta(t - t')$ for covariance σ_m^2 .

Equations 1-4 are solved by a Runge-Kutta Itô integrator implemented in the *sdeint* python package². The static pulsar parameters θ_{psr} are completely specified by our construction of the synthetic PTA outlined in Section 4.1.1. For this work we consider all pulsars to be observed for $T_{\text{obs}} = 10$ years, uniformly sampled with a weekly cadence. The measurement noise can be approximately related to the uncertainty in the pulse TOA, σ_{TOA} , as

$$\sigma_m \sim f_p^{(n)} \frac{\sigma_{\text{TOA}}}{\text{cadence}}. \quad (32)$$

For a millisecond pulsar with $f_p^{(n)} \sim 100$ Hz observed with a weekly cadence and $\sigma_{\text{TOA}} \sim 1 \mu\text{s}$ this gives $\sigma_m \sim 10^{-10}$, whilst the very best pulsars might have $\sigma_{\text{TOA}} \sim 10$ ns or $\sigma_m \sim 10^{-12}$. Throughout this work we fix $\sigma_m = 10^{-11}$ and it to be known *a priori* rather than a parameter to be inferred. Note that $f_m^{(n)}$ is modified by a different realisation of the measurement noise for each pulsar; whilst for our construction every pulsar is sampled at the same time and so would experience the same realisation of the noise, in actual pulsar astronomy different pulsars will be sampled at different times and so subject to different realisations of the measurement noise.

In practice, in order to avoid numerical precision issues that arise when solving Eq 1-4 (since $\sigma^{(n)} \ll f_p^{(n)}$) we first “heterodyne” our state by subtracting the deterministic frequency evolution, equivalent to a change of variables:

$$f_p'^{(n)} = f_p^{(n)} - f_{\text{em}}^{(n)} \quad (33)$$

We similarly heterodyne the measurement variable

$$f_m'^{(n)} = f_m^{(n)} - f_{\text{em}}^{*(n)} \quad (34)$$

¹ <https://github.com/meyers-academic/baboo>

² <https://github.com/mattja/sdeint>

where $f_{\text{em}}^{*(n)}$ is a guess of the deterministic spin-down based on the pulsar ephemeris. For synthetic data we can set $f_{\text{em}}^{*(n)} = f_{\text{em}}^{(n)}$ but this is not true generally for real-world observations since the spin-down ephemeris is only known approximately, not exactly. The measurement equation Eq. 16 that relates the state and measurement variables is then updated as

$$f_m^{(n)}(t) = f_p^{(n)}(t-d)g^{(n)}(t) - f_{\text{em}}^{(n)}((t-d))(1-g^{(n)}(t)) \quad (35)$$

We emphasise that this change of variables is simply a convenient scaling to bring our numerical values into a reasonable dynamic range without having to use extended numerical floating point formats (e.g. long double, quadruple). It does not remove any degrees of freedom of the formulation. In particular both $f_{\text{em}}^{(n)}(t_1)$ and $\dot{f}_{\text{em}}^{(n)}(t_1)$ remain static parameters of the model, but now appear in the measurement equation rather than the state equation.

4.2 Representative example

We initially characterise our method with a single example of a PTA which is perturbed by a GW from an individual quasi-monochromatic SMBHB source. The static GW source parameters θ_{gw} used for this injection are selected arbitrarily, subject to being astrophysically reasonable and representative. The injected θ_{gw} are summarised in the “Injected Values” column of Table 1. The static pulsar parameters θ_{psr} are as described in Section 4.1.1 and are also shown in Table 1.

4.2.1 Prior distributions

For the Bayesian methods used in this work, one must select reasonable priors, $\pi(\theta)$, for the complete set complete of static parameters. For $\pi(\theta_{\text{gw}})$ we choose standard non-informative priors (e.g. Bhagwat et al. 2021) as summarised in Table 1. The choice of $\pi(\theta_{\text{psr}})$ requires some additional discussion.

The parameters which govern the deterministic evolution of the pulsar spin frequency, $f_{\text{em}}^{(n)}(t_1), \dot{f}_{\text{em}}^{(n)}(t_1)$ are well-determined by existing radio timing observations. We can identify $f_{\text{em}}^{(n)}(t_1), \dot{f}_{\text{em}}^{(n)}(t_1)$ with the pulsar barycentric rotation frequency and the time derivative of barycentric rotation frequency quoted by pulsar observation catalogues. For the 12.5 year NANOGrav pulsars the mean error in the barycentric rotation frequency is $\sim 1.1 \times 10^{-11}$ Hz, and in the time derivative of barycentric rotation frequency is $\sim 1.29 \times 10^{-19} \text{ s}^{-2}$. These mean errors are skewed by a minority of pulsars which are less well timed; the median error in the barycentric rotation frequency is $\sim 7 \times 10^{-13}$ Hz, and in the time derivative of barycentric rotation frequency is $\sim 1.8 \times 10^{-20} \text{ s}^{-2}$. Whilst it is then clear that $f_{\text{em}}^{(n)}(t_1), \dot{f}_{\text{em}}^{(n)}(t_1)$ are typically measured with very high precisions, for this work we adopt a broader uniform prior, $\pm 1\%$ either side of the true value. In this way we can test how well our method performs without requiring exceptionally precise and accurate measurements of the pulsar parameters to be made *a priori*. Instead we consider the pulsar parameters similarly to the GW source parameters and estimate them optimally within a consistent framework.

The pulsar distances $d^{(n)}$ are typically not as well constrained as $f_{\text{em}}^{(n)}(t_1), \dot{f}_{\text{em}}^{(n)}(t_1)$, with uncertainties typically on the order of $\sim 10\%$ (Arzoumanian et al. 2018a; Yao et al. 2017). However for this work, whilst the pulsar distance is used when generating synthetic data, as discussed in Section 4.2.2 the pulsar distance is not used for our inference model and so we do not need to

Parameter	Injected Values	Units	Prior	
θ_{gw}	Ω	5×10^{-7}	Hz	LogUniform($10^{-9}, 10^{-5}$)
	α	1.0	radians	Uniform($0, 2\pi$)
	δ	1.0	radians	Cosine($-\pi/2, \pi/2$)
	ψ	2.50	radians	Uniform($0, 2\pi$)
	Φ_0	0.20	radians	Uniform($0, 2\pi$)
	h_0	10^{-12}	-	LogUniform($10^{-9}, 10^{-15}$)
	ι	1.0	radians	Sin($0, \pi$)
θ_{psr}	$f_{\text{em}}^{(n)}(t_1)$	$f_{\text{ATNF}}^{(n)}$	Hz	Uniform($0.9f_{\text{ATNF}}^{(n)}, 1.1f_{\text{ATNF}}^{(n)}$)
	$\dot{f}_{\text{em}}^{(n)}(t_1)$	$\dot{f}_{\text{ATNF}}^{(n)}$	s^{-2}	Uniform($0.9\dot{f}_{\text{ATNF}}^{(n)}, 1.1\dot{f}_{\text{ATNF}}^{(n)}$)
	$d^{(n)}$	$d_{\text{ATNF}}^{(n)}$	m	-
	$\sigma^{(n)}$	$\sigma_{\text{sc}}^{(n)}$?	LogUniform*($10^{-19}, 10^{-23}$)
	γ	10^{-13}	s^{-1}	-

Table 1. Summary of injected static parameters used for generating synthetic data in the representative example of Section 4.2, along with the choice of prior used for Bayesian inference on each parameter. The subscript “ATNF” denotes values which have been obtained from the ATNF pulsar catalogue as described in Section 4.1.1. The subscript “sc” indicates that the injected value has been calculated using the empirical timing model, Eq. 29, 30 from Shannon & Cordes (2010a). All pulsars use the prior on $\sigma^{(n)}$ as specified in the Table, with the exception of PSR J1939+2134 which uses LogUniform($10^{-15}, 10^{-17}$).

set a prior on d . Similarly we do not set a prior on $\gamma^{(n)}$; since $[\gamma^{(n)}]^{-1} \gg T_{\text{obs}}$ this means that $\gamma^{(n)}$ is effectively “unobservable” over the decadal timescales that we are interested in. That is, for $T_{\text{obs}} = 10$ years the solution of Eq 1 is effectively independent of the choice of $\gamma^{(n)}$ as long as the condition $[\gamma^{(n)}]^{-1} \gg T_{\text{obs}}$ is satisfied. It is therefore sufficient to consider $\gamma^{(n)}$ to be known *a priori* and set it at its true injected value. We briefly explored setting an uninformative prior on γ over e.g. LogUniform($10^{-10}, 10^{-15}$) as well as setting $\gamma^{(n)}$ at some fixed value away from the true injected value (e.g. set $\gamma^{(n)} = 10^{-14} \text{ s}^{-1}$ rather than 10^{-13} s^{-1}) but the results are unchanged. The majority of pulsars in our synthetic PTA have $\sigma^{(n)} \sim 10^{-20} - 10^{-22}$ as calculated from Eqs. 29, 30. For these pulsars we set an uninformative broad prior of LogUniform($10^{-19}, 10^{-23}$). The single exception is PSR J1939+2134 which has a particularly large $\dot{f}_p^{(n)}$ compared to the other pulsars in the array and so $\sigma \sim 10^{-16}$. For PSR J1939+2134 we set the prior at LogUniform($10^{-15}, 10^{-17}$).

Since we are not setting priors on γ or d this reduces the dimensionality of the parameter space to $7 + 3N$. We use the notation $\theta_{\text{psr, reduced}}$ to refer to the reduced parameter space. Explicitly,

$$\theta_{\text{psr, reduced}} = \left\{ f_{\text{em}}^{(n)}(t_1), \dot{f}_{\text{em}}^{(n)}(t_1), \sigma^{(n)} \right\}_{1 \leq n \leq N}, \quad (36)$$

All the injected static parameters and their corresponding priors for this representative example are summarised in Table 1.

4.2.2 Parameter estimation

From Eq. 18 it can be seen that the measurement equation generally separates into two cosine terms. The first term, $\cos(-\Omega t + \Phi_0)$, depends only on the GW source parameters and is shared across all pulsars. The argument of the cosine corresponds to the GW phase at the observer on Earth. Conversely the second term,

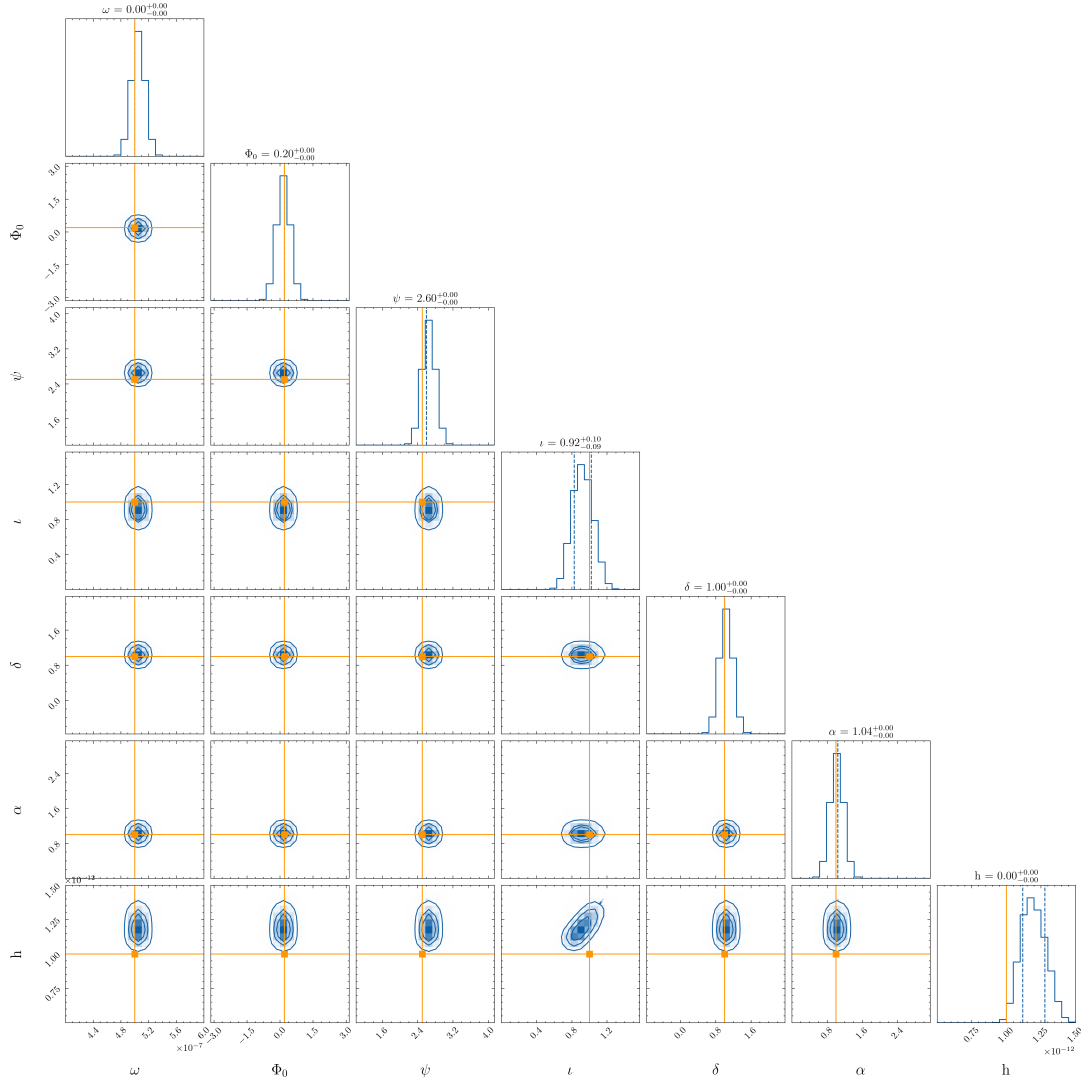


Figure 4. Posterior distribution for the GW source parameters θ_{gw} for a single realisation of the system noise. The vertical orange lines indicate the true injected values, c.f. Table 1. The contours in the 2D histograms denote the (0.5, 1, 1.5, 2)- σ levels. We are able to accurately estimate each parameter of interest.

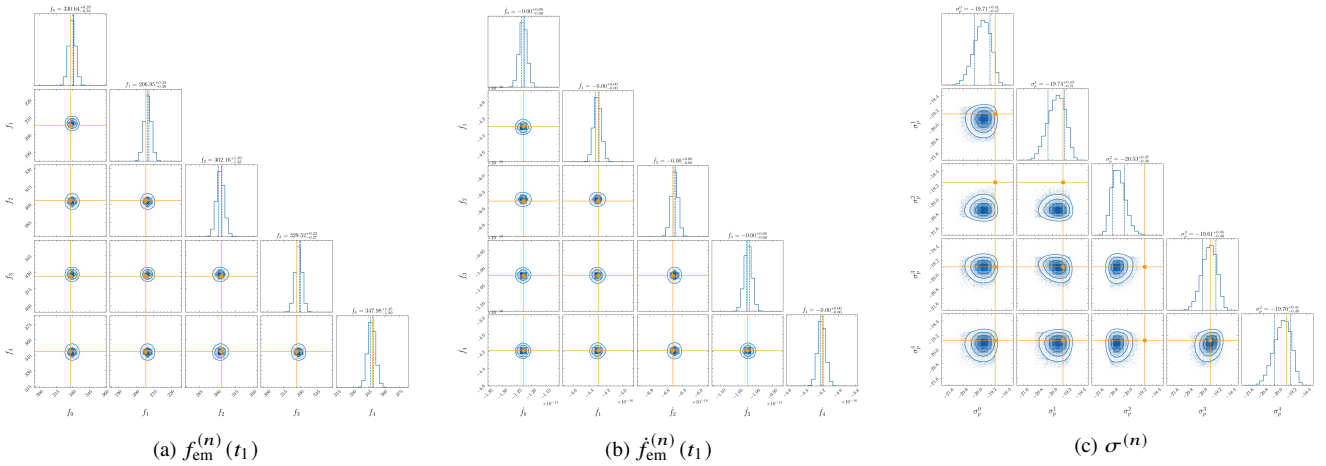


Figure 5. As Fig 4 but for the $3N$ pulsar parameters $\theta_{\text{psr, reduced}}$. We show only a selection of the first 5 pulsars rather than the full PTA.

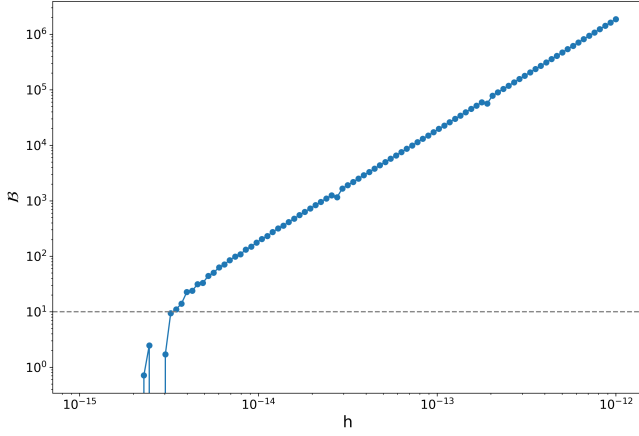


Figure 6. Bayes ratio β between the competing models M_∞ (GW present in data) and M_0 (GW not present in data) at different GW strain magnitudes, h_0 , for the representative example summarised in Table 1. The horizontal grey dashed line labels the detection tolerance cut-off of $\beta = 10$. The minimal detectable strain, below which $\beta < 10$, is $\sim 3 \times 10^{-15}$.

5 DISCUSSION

hellings downs

multiple sources

spherical localisatin plot would be cool e.g.

<https://github.com/stephengreen/lfi-gw>

comparison with alternative methods

Points to discuss:

- Non constant time sampling? Different pulsars sampled at different times...
- pulsar terms obv

6 CONCLUSION

Our method is not contingent on the choice of PTA, and naturally extend to other PTAs or PTAs with more pulsars.

Questions

- PTAs like MSPs for small timing noise. Can we get away with large timing noise, and use more pulsars? Some pulsars are more useful than others, e.g. arXiv 2211.03201
- Can we also estimate radiometer noise? Is this useful?

APPENDIX A: KALMAN RECURSION EQUATIONS

The linear Kalman filter operates on temporally discrete measurements which are related to unobservable system states via a linear transformation

$$\bar{z} = \bar{H}\bar{x} + \bar{v} \quad (\text{A1})$$

where \bar{H} is the measurement matrix and \bar{v} is a Gaussian measurement noise. The underlying states evolve according to are the state-space dynamical equation

$$\dot{\bar{x}} = \bar{F}\bar{x} + \bar{G}\bar{u} + \bar{w} \quad (\text{A2})$$

for the system dynamics matrix, \bar{F} , control model G , control vector \bar{u} , and w a stochastic zero-mean process. By comparison with the preceding equations, Eqs. A9 - ??, it is immediately obvious how our state space model maps onto the Kalman filter structure. Specifically, our states are just the N intrinsic pulsar frequencies $\bar{x} = (f_1, f_2, \dots, f_N)$ whilst our measurements are the N measured pulse frequencies $\bar{z} = (f_1^{(M)}, f_2^{(M)}, \dots, f_N^{(M)})$. If we specialize to the case of constant time sampling between our observations, Δt , then for our formulation the components that make up the Kalman filter are as follows:

$$F_i = F_{i+1} = e^{-\gamma \Delta t} \quad (\text{A3})$$

$$T_i = \int_{t_i}^{t_{i+1}} e^{A(t_{i+1}-t')} N(t') dt' \quad (\text{A4})$$

$$= f_{\text{EM}}(0) + \dot{f}_{\text{EM}}(0)(\Delta t + t_i) - e^{-\gamma \Delta t} (f_{\text{EM}}(0) + \dot{f}_{\text{EM}}(0)t_i) \quad (\text{A5})$$

$$H_i = 1 - A(\theta_{\text{GW}}) \cos(-\Omega t_i(1 + n \cdot q) + \Phi_0) \quad (\text{A6})$$

where the i subscript labels the value at the i -th timestep, and A is a constant that is given by Eq. ??.

The Kalman filter includes the effect of process noise \bar{w} and the measurement noise \bar{v} via the definition of a process noise matrix $Q = E[ww^T]$ and a measurement noise matrix $R = E[vv^T]$, which have the discrete form,

$$Q_i \delta_{ij} = \langle \eta_i \eta_j^T \rangle = \frac{-\sigma^2}{2\gamma} (e^{-2\gamma \Delta t} - 1) \quad (\text{A7})$$

$$R_i = R_{i+1} = \Sigma^2 \quad (\text{A8})$$

The above equations, Eqs. A3 - A8, apply to an operation on a single state. The extension to N states is straightforward, since one just needs to construct a diagonal matrix for each of the Kalman components where each non-zero element corresponds to a separate pulsar frequency.

In Section ?? we present a discretised version of the model of Section 2 which maps onto the discretely sampled observable $f(\tau)|_{\text{Earth}}$.

In order to make contact with discretely sampled data it is important to temporally discretise the model of Section 2

We can express the intrinsic frequency evolution, Eq. ??, in an alternative form as, **TK all this needs updating**

$$df = \gamma f dt + N(t)dt + \sigma dB(t) \quad (\text{A9})$$

where $\mathcal{A} = -\gamma$, $N(t) = \gamma(f_{\text{EM}}(0) + \dot{f}_{\text{EM}}(0)t) + \dot{f}_{\text{EM}}(0)$ and $dB(t)$ denotes increments of Brownian motion (Wiener process). This equation is easily identified as an Ornstein-Uhlenbeck process which has a general solution given by (Gardiner 2009),

$$f(t) = e^{\mathcal{A}t} f(0) + \int_0^t e^{\mathcal{A}(t-t')} N(t') dt' + \int_0^t e^{\mathcal{A}(t-t')} \sigma dB(t')$$

(A10)

If we move from a solution in continuous time, t , to discrete time, **TK: AM recommends deligint tabe sy,bol** $\bar{t} = (t_1, t_2, \dots, t_K)$, then

$$f(t_{i+1}) = Ff(t_i) + T_i + \eta_i \quad (\text{A11})$$

where

$$F_i = e^{\mathcal{A}(t_{i+1}-t_i)} \quad (\text{A12})$$

$$T_i = \int_{t_i}^{t_{i+1}} e^{\mathcal{A}(t_{i+1}-t')} N(t') dt' \quad (\text{A13})$$

$$\eta_i = \int_{t_i}^{t_{i+1}} e^{\mathcal{A}(t_{i+1}-t')} \sigma dt' \quad (\text{A14})$$

if we specialise to the case of constatin time sampling

The discrete solution $f(\bar{t})$ to the intrinsic frequency can be related to the discrete measured frequency via Eq. ?? as,

$$f_M(\bar{t}) = f(\bar{t})g(\bar{\theta}, \bar{t}) + N_M \quad (\text{A15})$$

where $g(\theta, t)$ can be expressed in a trigonometric form as

$$X = 1 - \frac{1}{2} \frac{H_{ij} q^i q^j}{(1 + \bar{n} \cdot \bar{q})} [\cos(-\Omega\tau + \Phi_0) - \cos(-\Omega\tau + \Phi_0 + \Omega(1 + \bar{n} \cdot \bar{q})d)] \quad (\text{A16})$$

whilst N_M is a Gaussian measurement noise that satisfies

$$\langle N_M(t) N_M(t') \rangle = \Sigma^2 \delta(t - t') \quad (\text{A17})$$

for variance Σ^2 .

A1 References

REFERENCES

- Agazie G., et al., 2023a, *ApJ*, **951**, L8
 Agazie G., et al., 2023b, *ApJ*, **951**, L9
 Alam M. F., et al., 2021, *ApJS*, **252**, 4
 Allen B., 1997, in Marck J.-A., Lasota J.-P., eds, *Relativistic Gravitation and Gravitational Radiation*. pp 373–417 ([arXiv:gr-qc/9604033](#), [doi:10.48550/arXiv.gr-qc/9604033](#))
 Antonelli M., Basu A., Haskell B., 2023, *MNRAS*, **520**, 2813
 Antoniadis J., et al., 2022, *MNRAS*, **510**, 4873
 Antoniadis J., et al., 2023a, *arXiv e-prints*, p. [arXiv:2306.16214](#)
 Antoniadis J., et al., 2023b, *arXiv e-prints*, p. [arXiv:2306.16224](#)
 Antoniadis J., et al., 2023c, *arXiv e-prints*, p. [arXiv:2306.16226](#)
 Arzoumanian Z., et al., 2018a, *ApJS*, **235**, 37
 Arzoumanian Z., et al., 2018b, *ApJ*, **859**, 47
 Arzoumanian Z., et al., 2020a, *ApJ*, **900**, 102
 Arzoumanian Z., et al., 2020b, *ApJ*, **905**, L34
 Arzoumanian Z., et al., 2023, *arXiv e-prints*, p. [arXiv:2301.03608](#)
 Ashton G., Talbot C., 2021, *MNRAS*, **507**, 2037
 Ashton G., et al., 2022, *Nature Reviews Methods Primers*, **2**, 39
 Babak S., Sesana A., 2012, *Phys. Rev. D*, **85**, 044034
 Babak S., et al., 2016, *MNRAS*, **455**, 1665
 Bailes M., et al., 2020, *Publications of the Astronomical Society of Australia*, **37**, e028
 Baym G., Pethick C., Pines D., Ruderman M., 1969, *Nature*, **224**, 872
 Bhagwat S., De Luca V., Franciolini G., Pani P., Riotto A., 2021, *J. Cosmology Astropart. Phys.*, **2021**, 037
 Brook P. R., Karastergiou A., Buchner S., Roberts S. J., Keith M. J., Johnston S., Shannon R. M., 2013, *The Astrophysical Journal Letters*, **780**, L31
 Buchner J., 2021a, *arXiv e-prints*, p. [arXiv:2101.09675](#)
 Buchner J., 2021b, *The Journal of Open Source Software*, **6**, 3001
 Burke-Spolaor S., et al., 2019, *A&ARv*, **27**, 5
 Caballero R. N., et al., 2016, *MNRAS*, **457**, 4421
 Charisi M., Taylor S. R., Witt C. A., Runnoe J., 2023, *arXiv e-prints*, p. [arXiv:2304.03786](#)
 Chen J.-W., Wang Y., 2022, *ApJ*, **929**, 168
 Christensen N., 2019, *Reports on Progress in Physics*, **82**, 016903
 Cordes J. M., Greenstein G., 1981, *ApJ*, **245**, 1060
 Cordes J. M., Lazio T. J. W., 2002, *arXiv e-prints*, pp astro-ph/0207156
 Cordes J. M., Shannon R. M., 2010, *arXiv e-prints*, p. [arXiv:1010.3785](#)
 D'Alessandro F., McCulloch P. M., Hamilton P. A., Deshpande A. A., 1995, *MNRAS*, **277**, 1033
 Desvignes G., et al., 2016, *Monthly Notices of the Royal Astronomical Society*, **458**, 3341
 Dunn L., et al., 2022, *MNRAS*, **512**, 1469
 Dunn L., Melatos A., Espinoza C. M., Antonopoulou D., Dodson R., 2023, *MNRAS*, **522**, 5469
 Ellis J. A., 2013, *Classical and Quantum Gravity*, **30**, 224004
 Ellis J. A., Cornish N. J., 2016, *Phys. Rev. D*, **93**, 084048
 Ellis J. A., Siemens X., Creighton J. D. E., 2012, *ApJ*, **756**, 175
 Espinoza C. M., Antonopoulou D., Dodson R., Stepanova M., Scherer A., 2021, *A&A*, **647**, A25
 Feroz F., Hobson M. P., 2008, *MNRAS*, **384**, 449
 Feroz F., Hobson M. P., Bridges M., 2009, *Monthly Notices of the Royal Astronomical Society*, **398**, 1601
 Gardiner C., 2009, *Stochastic Methods: A Handbook for the Natural and Social Sciences*. Springer Series in Synergetics, Springer Berlin Heidelberg, [https://books.google.com.au/books?id=otg3PQAACAAJ](#)
 Goldstein J. M., Veitch J., Sesana A., Vecchio A., 2018, *MNRAS*, **477**, 5447
 Goncharov B., et al., 2021, *MNRAS*, **502**, 478
 Greenstein G., 1970, *Nature*, **227**, 791
 Gügercinoğlu E., Alpar M. A., 2017, *MNRAS*, **471**, 4827
 Handley W. J., Hobson M. P., Lasenby A. N., 2015, *MNRAS*, **450**, L61
 Hellings R. W., Downs G. S., 1983, *ApJ*, **265**, L39
 Hobbs G., Lyne A. G., Kramer M., 2010, *MNRAS*, **402**, 1027
 Hobbs G., Dai S., Manchester R. N., Shannon R. M., Kerr M., Lee K.-J., Xu R.-X., 2019, *Research in Astronomy and Astrophysics*, **19**, 020
 Jaffe A. H., Backer D. C., 2003, *The Astrophysical Journal*, **583**, 616
 Jenet F. A., Lommen A., Larson S. L., Wen L., 2004, *ApJ*, **606**, 799
 Johnston S., Galloway D., 1999, *Monthly Notices of the Royal Astronomical Society*, **306**, L50
 Jones P. B., 1990, *MNRAS*, **246**, 364
 Kalman R. E., 1960, *Journal of Basic Engineering*, **82**, 35
 Kerr M., Hobbs G., Johnston S., Shannon R. M., 2015, *Monthly Notices of the Royal Astronomical Society*, **455**, 1845
 Kramer M., Lyne A. G., O'Brien J. T., Jordan C. A., Lorimer D. R., 2006, *Science*, **312**, 549
 Lam M. T., et al., 2019, *ApJ*, **872**, 193
 Lasky P. D., Melatos A., Ravi V., Hobbs G., 2015, *MNRAS*, **449**, 3293
 Lee K. J., Wex N., Kramer M., Stappers B. W., Bassa C. G., Janssen G. H., Karuppusamy R., Smits R., 2011, *MNRAS*, **414**, 3251
 Lentati L., et al., 2015, *MNRAS*, **453**, 2576
 Lower M. E., et al., 2021, *MNRAS*, **508**, 3251
 Lyne A., Hobbs G., Kramer M., Stairs I., Stappers B., 2010, *Science*, **329**, 408
 Maggiore M., 2018, *Gravitational Waves: Volume 2: Astrophysics and Cosmology*. Oxford University Press, [doi:10.1093/oso/9780198570899.001.0001](#), [https://doi.org/10.1093/oso/9780198570899.001.0001](#)
 Manchester R. N., Hobbs G. B., Teoh A., Hobbs M., 2005, *AJ*, **129**, 1993
 McWilliams S. T., Ostrikor J. P., Pretorius F., 2014, *The Astrophysical Journal*, **789**, 156
 Melatos A., Link B., 2014, *MNRAS*, **437**, 21
 Melatos A., Peralta C., Wyithe J. S. B., 2008, *ApJ*, **672**, 1103
 Melatos A., Dunn L. M., Suvorova S., Moran W., Evans R. J., 2020, *ApJ*, **896**, 78
 Melatos A., O'Neill N. J., Meyers P. M., O'Leary J., 2021, *MNRAS*, **506**, 3349
 Meyers P. M., Melatos A., O'Neill N. J., 2021a, *MNRAS*, **502**, 3113

- Meyers P. M., O'Neill N. J., Melatos A., Evans R. J., 2021b, *MNRAS*, **506**, 3349
- Mukherjee P., Parkinson D., Liddle A. R., 2006, *ApJ*, **638**, L51
- Pártay L. B., Bartók A. P., Csányi G., 2009, *arXiv e-prints*, p. arXiv:0906.3544
- Parthasarathy A., et al., 2021, *MNRAS*, **502**, 407
- Peralta C., Melatos A., Giacobello M., Ooi A., 2006, *ApJ*, **651**, 1079
- Perera B. B. P., et al., 2019, *MNRAS*, **490**, 4666
- Petiteau A., Babak S., Sesana A., de Araújo M., 2013, *Phys. Rev. D*, **87**, 064036
- Pitkin M., 2018, *Journal of Open Source Software*, **3**, 538
- Rajagopal M., Romani R. W., 1995, *ApJ*, **446**, 543
- Ravi V., Wyithe J. S. B., Hobbs G., Shannon R. M., Manchester R. N., Yardley D. R. B., Keith M. J., 2012, *ApJ*, **761**, 84
- Ravi V., Wyithe J. S. B., Shannon R. M., Hobbs G., 2015, *MNRAS*, **447**, 2772
- Reardon D. J., et al., 2023, *ApJ*, **951**, L6
- Renzini A. I., Goncharov B., Jenkins A. C., Meyers P. M., 2022, *Galaxies*, **10**, 34
- Rosado P. A., Sesana A., Gair J., 2015, *Monthly Notices of the Royal Astronomical Society*, **451**, 2417
- Sanidas S. A., Battye R. A., Stappers B. W., 2012, *Phys. Rev. D*, **85**, 122003
- Sesana A., 2013, *Classical and Quantum Gravity*, **30**, 224014
- Sesana A., Vecchio A., 2010, *Phys. Rev. D*, **81**, 104008
- Sesana A., Vecchio A., Colacino C. N., 2008, *Monthly Notices of the Royal Astronomical Society*, **390**, 192
- Shannon R. M., Cordes J. M., 2010a, *ApJ*, **725**, 1607
- Shannon R. M., Cordes J. M., 2010b, *ApJ*, **725**, 1607
- Shannon R. M., et al., 2013, *The Astrophysical Journal*, **766**, 5
- Simon D., 2006, *Optimal State Estimation: Kalman, H Infinity, and Nonlinear Approaches*. Wiley-Interscience, USA
- Skilling J., 2006, *Bayesian Analysis*, **1**, 833
- Sornette D., 2004, *Critical phenomena in natural sciences : chaos, fractals selforganization and disorder : concepts and tools*
- Speagle J. S., 2020, *Monthly Notices of the Royal Astronomical Society*, **493**, 3132
- Spiewak R., et al., 2022, *Publ. Astron. Soc. Australia*, **39**, e027
- Stairs I. H., Lyne A. G., Shemar S. L., 2000, *Nature*, **406**, 484
- Stairs I. H., et al., 2019, *MNRAS*, **485**, 3230
- Sykes B., Middleton H., Melatos A., Di Matteo T., DeGraf C., Bhowmick A., 2022, *MNRAS*, **511**, 5241
- Tarafdar P., et al., 2022, *Publications of the Astronomical Society of Australia*, **39**, e053
- Taylor S. R., Huerta E. A., Gair J. R., McWilliams S. T., 2016, *ApJ*, **817**, 70
- Tiburzi C., 2018, *Publ. Astron. Soc. Australia*, **35**, e013
- Trassinelli M., 2019, *Proceedings*, **33**
- Urama J. O., Link B., Weisberg J. M., 2006, *MNRAS*, **370**, L76
- Vargas A., Melatos A., 2023, *TBD*, **1**, 1
- Verbiest J. P. W., Weisberg J. M., Chael A. A., Lee K. J., Lorimer D. R., 2012, *ApJ*, **755**, 39
- Verbiest J. P. W., Osłowski S., Burke-Spolaor S., 2021, in , *Handbook of Gravitational Wave Astronomy*. p. 4, doi:10.1007/978-981-15-4702-7_4-1
- Wan E., Van Der Merwe R., 2000, in *Proceedings of the IEEE 2000 Adaptive Systems for Signal Processing, Communications, and Control Symposium (Cat. No.00EX373)*. pp 153–158, doi:10.1109/ASSPCC.2000.882463
- Wyithe J. S. B., Loeb A., 2003, *ApJ*, **590**, 691
- Xu H., et al., 2023, *Research in Astronomy and Astrophysics*, **23**, 075024
- Xue X., et al., 2021, *Phys. Rev. Lett.*, **127**, 251303
- Yao J. M., Manchester R. N., Wang N., 2017, *ApJ*, **835**, 29
- Yardley D. R. B., et al., 2010, *MNRAS*, **407**, 669
- Zarchan P., Musoff H., 2000, *Fundamentals of Kalman Filtering: A Practical Approach*. Progress in astronautics and aeronautics, American Institute of Aeronautics and Astronautics, <https://books.google.com.au/books?id=AQxRAAAMAAJ>
- Zhu X. J., et al., 2014, *MNRAS*, **444**, 3709
- Zhu X.-J., et al., 2015a, *Monthly Notices of the Royal Astronomical Society*, **449**, 1650
- Zhu X.-J., et al., 2015b, *Monthly Notices of the Royal Astronomical Society*, **449**, 1650
- Zhu X.-J., Wen L., Xiong J., Xu Y., Wang Y., Mohanty S. D., Hobbs G., Manchester R. N., 2016, *Monthly Notices of the Royal Astronomical Society*, **461**, 1317
- Zic A., et al., 2023, *arXiv e-prints*, p. arXiv:2306.16230
- van Eysden C. A., Melatos A., 2010, *MNRAS*, **409**, 1253

This paper has been typeset from a \LaTeX file prepared by the author.